Scaling Effects of an Aerodynamic Plasma Actuator

Mehul P. Patel,[*] T. Terry Ng,[†] and Srikanth Vasudevan[‡]
Orbital Research Inc., Cleveland, Ohio 44103-3733
Thomas C. Corke[§]
University of Notre Dame, Notre Dame, Indiana 46556
Martiqua L. Post[¶] and Thomas E. McLaughlin[**]
U. S. Air Force Academy,
Colorado Springs, Colorado 80840-6222
and
Charles F. Suchomel[††]
U.S. Air Force Research Laboratory,
Wright–Patterson Air Force Base, Dayton, Ohio 45433

We present experimental results to yield insight into the scalability and control effectiveness of single-dielectric-barrier-discharge plasma actuators for leading-edge separation control on airfoils. The parameters investigated are chord Reynolds number, Mach number, leading-edge radius, actuator amplitude, and unsteady frequency. This includes chord Reynolds numbers up to 1.0×10^6 and a maximum freestream speed of 60 m/s corresponding to a Mach number of 0.176. The main objective of this work is to examine the voltage requirements for the plasma actuators to reattach the flow at the leading edge of airfoils at poststall angles of attack for a range of flow parameters in order to establish scaling between laboratory and full-flight conditions. For the full range of conditions, an optimum unsteady actuator frequency f is found to minimize the actuator voltage needed to reattach the flow, such that $F^+ = f L_{\text{sep}}/U_\infty = 1$. At the optimum frequencies, the minimum voltage required to reattach the flow is weakly dependent on chord Reynolds number and strongly dependent on the poststall angle of attack and leading-edge radius. The results indicate that the voltage required to reattach the flow scales as the square of the leading-edge radius.

Nomenclature

α	=	angle of attack, deg
α_s	=	stall angle of attack, deg
b	=	airfoil span, m
C_L	=	lift coefficient
c	=	airfoil chord, m
F^+	=	nondimensional frequency of the actuator
f	=	modulation frequency, Hz
L_{sep}	=	streamwise extent of the separation zone, m
M	=	Mach number
Re	=	Reynolds number
Re_c	=	Reynolds number based on the mean chord and freestream velocity
r_{LE}	=	airfoil leading-edge radius, m
St	=	Strouhal number based on the mean chord
t	=	airfoil thickness, m

U_∞	=	freestream velocity at entrance to the test section, m/s
x	=	distance from the leading edge, m
y	=	spanwise distance from the centerline, m

*Director, Aerodynamics Group, 4415 Euclid Avenue, Suite 500. Senior Member AIAA.
†Chief Aerodynamicist, 4415 Euclid Avenue, Suite 500. Senior Member AIAA.
‡Aerospace Engineer, 4415 Euclid Avenue, Suite 500. Member AIAA.
§Clark Chair Professor, Aerospace and Mechanical Engineering Department, 101 Hessert Laboratory for Aerospace Research. Associate Fellow AIAA.
¶Assistant Professor, Department of Aeronautics. Senior Member AIAA.
**Director, Aeronautics Research Center. Associate Fellow AIAA.
††Program Manager, Air Vehicles Directorate. Associate Fellow AIAA.

I. Introduction

THERE is a growing interest in the development of plasma actuators for aerodynamic applications for both low and high speeds. A number of different plasma actuators have been considered for controlling fluid flow phenomena, including dielectric barrier discharge (DBD) [1,2], dc glow discharge [3], radio-frequency glow discharge [4], and filamentary arc discharge [5]. Suchomel et al. [6] provide an overview of different plasma technologies currently under investigation for aeronautical applications. This paper focuses on the DBD plasma actuator, in particular, the single-dielectric-barrier-discharge (SDBD) configuration [1]. We present experimental results to yield insight into the scalability and control effectiveness of the SDBD plasma actuator as a function of different parameters, including chord Reynolds numbers (Re_c up to 1.0×10^6), Mach numbers (up to 0.176), leading-edge radius, actuator amplitude, and unsteady frequency. The main objective of this work is to examine the voltage requirements for the plasma actuators to reattach the flow at the leading edge of airfoils at poststall angles of attack for a large range of flow parameters to establish scaling between the laboratory and full-flight conditions.

II. Aerodynamic Plasma Actuator

In the SDBD configuration, the actuator consists of two asymmetrically overlapped metal electrodes, separated by a dielectric material, as illustrated in Fig. 1. The upper electrode is exposed to the surrounding air and the lower (covered) electrode is fully insulated. When a sufficiently high-amplitude ac voltage is supplied to the electrodes, the air over the covered electrode ionizes. The ionized air is referred to as the plasma. The basis of this actuator is that the plasma, in the presence of the electric field gradient
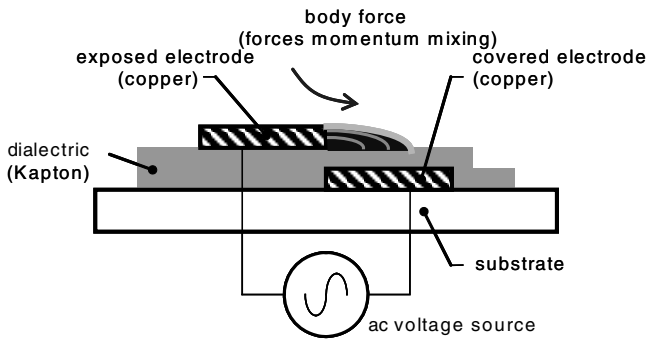
Fig. 1 Schematic of a SDBD plasma actuator.

produced by the electrode geometry, results in a body force vector that acts on the ambient air [7,8]. The body force vector induces flow in a way that might be thought of as resulting from a virtual change in the aerodynamic shape. The body force is proportional to the ac voltage amplitude and the volume of plasma. It can be tailored for a given application by configuring the orientation and design of the electrode geometry. The body force representation is also a convenient form to incorporate the effect of the actuators into Navier–Stokes flow simulations. Such codes are currently being used to design, predict, and optimize the performance of plasma actuators for various applications [9–11].

An excellent review of the physics and the underlying mechanisms of the aerodynamic plasma actuator is provided by Enloe et al. [7,8]. It is important to note that the SDBD plasma-actuator design has a self-limiting property and therefore is stable even at atmospheric pressures. Until recent years, the use of DBDs was limited to industrial processes; however, with recent demonstrations of a SDBD as an aerodynamic plasma actuator, researchers have been motivated to develop the SDBD actuator for various flow control applications. The use of an aerodynamic plasma actuator as a wing flow control device is particularly appealing due to its low-cost, lightweight, flexible design with no moving parts. The SDBD actuators in these applications require very-low-power devices with typical power levels of approximately 20–40 W per linear foot of actuator span for steady operation and 2–4 W per linear foot of actuator span for unsteady operation.

The use of SDBD plasma actuators for flow control has been demonstrated in many applications. Examples include boundary-layer control [12], lift augmentation on wings [13], separation control for low-pressure turbine blades [14], leading-edge separation control on wing sections [15], phased plasma arrays for unsteady flow control [16], and control of the dynamic stall vortex on oscillating airfoils [17]. In the recent past, the authors have demonstrated the use of plasma actuators for high-lift aircraft applications such as plasma flaps and slats [18], smart plasma slats [19], and plasma wings for hingeless control [20–22].

In previous work conducted on a two-dimensional NACA 0015 airfoil at chord Reynolds numbers Re_c of 0.18×10^6, 0.217×10^6, and 0.307×10^6, we showed that plasma actuators are highly effective in controlling flow separation and delaying wing stall using unsteady excitations that are scaled with the natural vortex-shedding frequency, predicted using a reduced frequency, $F^+ = fL_{sep}/U_\infty = 1$. Here, f is the unsteady actuator forcing frequency, L_{sep} is the streamwise extent of flow separation (which, in the case of a full leading-edge separation, is the airfoil chord length c), and U_∞ is the freestream velocity. Results from unsteady-frequency-sensitivity tests conducted on other 2-D airfoil section shapes since then support the optimum conditions at $F^+ \simeq 1$. It has also been shown in the literature that the introduction of unsteady disturbances near the separation location can cause the generation of large coherent vortical structures that could prevent or delay the onset of separation. These structures are thought to bring high-momentum fluid to the surface, enabling the flow to withstand the adverse pressure gradient without separating. Periodic excitation by oscillatory blowing for use in separation control has been documented extensively by

Seifert et al. [23–26] and in the review by Greenblatt and Wygnanski [27].

One of the other benefits of unsteady actuation is that actuator power requirements can be significantly reduced. In the unsteady forcing, very short duty cycles (as small as 10%) were found to be effective. This then reduces the power by as much as 90% over steady plasma-actuator operation. Although there have been many demonstrations of SDBD actuators for separation-control applications, many of these have focused on lower-Reynolds-number flows. The motivation of the present work is to present experimental evidence of a plasma actuator for use as a performance-enhancing device for speeds up to Re_c of 1.0×10^6 and a maximum U_∞ of 60 m/s corresponding to 0.176×10^6. This would allow minimization or elimination of traditional movable control surfaces for flight control during typical aircraft takeoff and landing speeds. A good understanding of the plasma actuator's control authority and performance as a flow control device for controlling flow separation at high-Reynolds-number flows is lacking. To date, only a few experimental or computational data on the effects of the SDBD actuator for high-Reynolds-number flows are available. In a
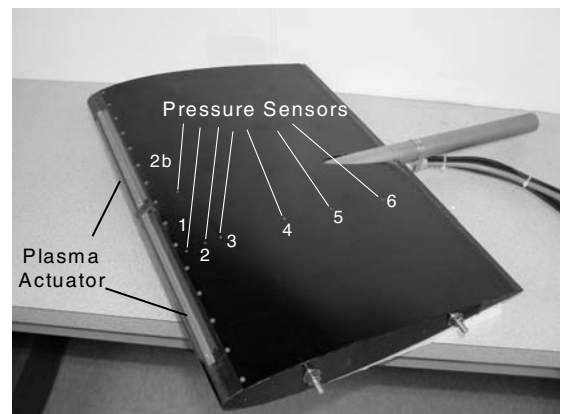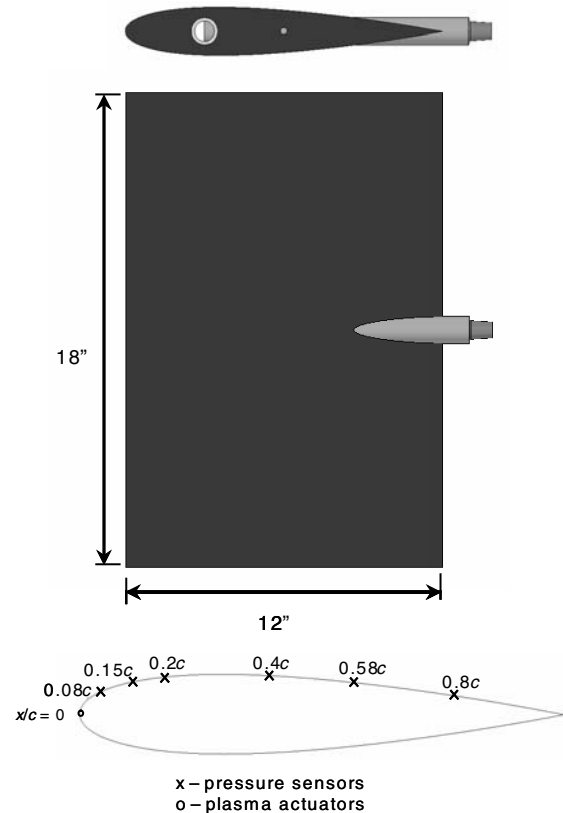

Fig. 2 Illustrations of the NACA 0015 airfoil model with pressure sensors and leading-edge plasma actuators used in experiments.

computational study performed by Corke et al. [28] on a high-speed natural laminar flow airfoil, HSNLF(1)-0213, SDBD actuators were shown to produce changes in lift comparable with that of a moving flap at Mach 0.69. In another experimental study, conducted parallel to the present work, on the same airfoil section shape HSNLF(1)-0213, Post et al. [29] demonstrated the effect of a plasma actuator (oriented upstream) on aerodynamic lift at Mach 0.1 and 0.2.

Although many researchers are currently involved in investigating the physics and applications of these devices, to what degree the plasma actuators are effective in affecting flows at typical aircraft speeds is yet to be ascertained. Further work is needed to fully understand the fundamental processes governing the interaction of the SDBD actuator and its potential for high-Reynolds-number-flow applications. Our approach to further this study is to conduct wind-tunnel experiments to develop scaling laws that define the actuator behavior for different flow conditions.

III. Leading-Edge Separation-Control Scaling: NACA 0015

The problem of controlling leading-edge separation was chosen as the test case for this study. The airfoil used in the first study was a two-dimensional NACA 0015 that had a 30.48-cm (12-in.) chord and a 45.72-cm (18-in.) span. The size of the airfoil was chosen to provide high chord Reynolds numbers with minimum blockage effects. This shape was chosen because it was the subject of earlier experiments on the control of steady and dynamic stall using plasma actuators [15,18,19]. The NACA 0015 airfoil skin was made out of 0.16-cm-thick carbon fiber sheet, and the internal structure was

a)

b)

Fig. 3 Photographs of the NACA 0015 airfoil model used in experiments.

supported by ribs made of carbon fiber and fiberglass. Two steel rods welded to form a T-joint reinforced the airfoil components (ribs and the main spar) and was also used for mounting on the sting. Inverted C-clamps were used to strengthen the steel T-support rods to reduce bending effects. The airfoil was instrumented with six high-bandwidth pressure sensors and a leading-edge plasma actuator. The actuator was a split-design located side by side at $x/c = 0$, covering 80% of the wing span. Both actuators were controlled together, in phase, to create the effect of a single long actuator. A signal-conditioning unit for the dynamic pressure sensors was housed inside the airfoil, aft of the spanwise support rod. Transformers to run the plasma actuators were placed inside the airfoil to reduce interference with the data acquisition. Figure 2 shows details of the airfoil and chord locations of the pressure sensors and SDBD actuators.

A. Experimental Setup

Wind-tunnel experiments were conducted in a 2.133 m long, 0.9 by 0.9 m (7 ft long and 3 by 3 ft) subsonic wind tunnel at the U.S. Air Force Academy. Figure 3 shows photographs of the 0015 airfoil mounted inside the wind tunnel. Figure 3a shows the airfoil with the actuator off and Fig. 3b shows the airfoil with the actuator on. Figure 4 shows a photograph of the airfoil setup inside the wind tunnel. This closed-circuit single-return wind tunnel has an operating range between 15 and 183 m/s, which is a maximum Mach number of 0.6. The wind tunnel contains a drive system with a 1000-hp induction motor, a 9-ft-diam axial flow fan, and a variable-frequency drive. The flow quality offered less than 0.2% turbulence intensity. The model was supported using a sting mount on a arc-center turntable with ± 28- deg pitch control. The model was controlled and measured remotely using a HP 3852A data acquisition system. Access for running electronic cables for the pressure sensors and the actuators was provided downstream of the test section. Clear glass panels on the side and top of the test section provided optical access. Transformers for the actuators were placed directly inside the airfoil and therefore no high-voltage wires were run through the tunnel.
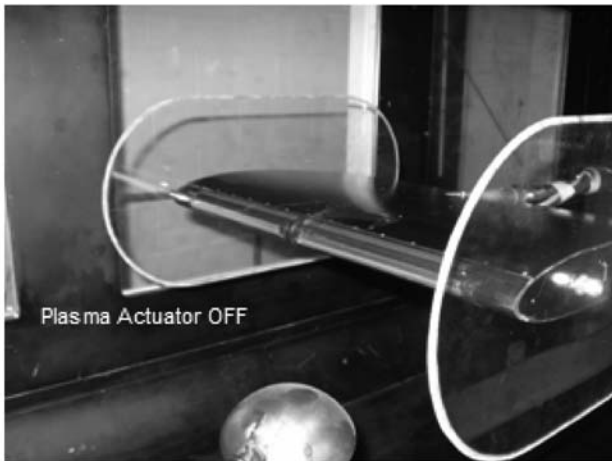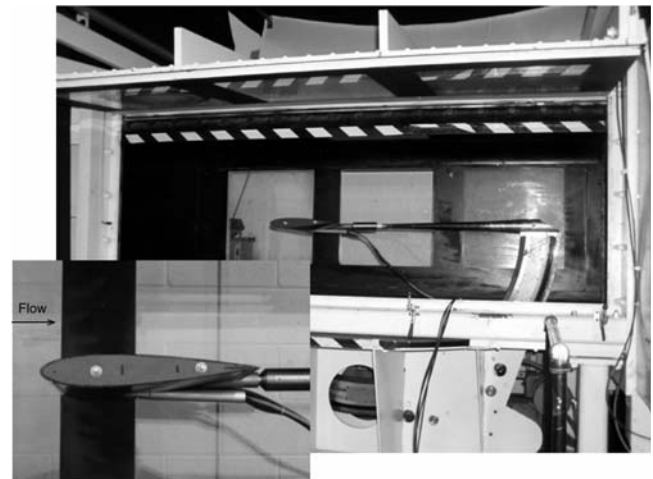

Fig. 4 Photograph of 0015 model mounted inside the U.S. Air Force Academy (USAFA) subsonic wind tunnel. A small tube carrying wires for the pressure sensors and the plasma actuators underneath the sting support is shown.
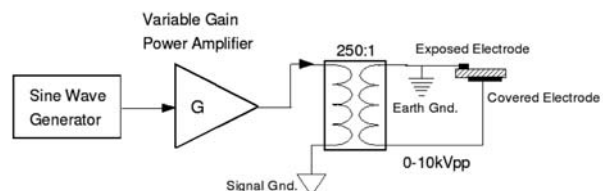

Fig. 5 Electronics circuit used to generate the plasma.

Re	M	U_∞, m/s	AOA, deg
383,809	0.068	23	20
417,184	0.073	25	20, 21, 22, 23, 24
450,559	0.079	27	20
500,621	0.088	30	14–22
517,308	0.091	31	17.5, 19.5, 20
584,058	0.103	35	14–22
609,089	0.107	36	18
634,120	0.112	38	18
667,494	0.118	40	14–22
750,931	0.132	45	14–22
800,993	0.141	48	21
834,369	0.147	50	14–22
917,806	0.162	55	14–22
1,000,000	0.176	60	14–22

This eliminated electromagnetic interference with the data acquisition signal, which was verified by monitoring the noise (or lack thereof) in the data by turning the actuator off and on. A 250-lb force balance mounted on the sting was used for the experiments.

A single-dielectric-barrier-discharge plasma actuator was used on the leading edge ($x/c = 0$) to mitigate flow separation. The plasma actuators were made from two 0.0254-mm-thick copper electrodes separated by two 0.1-mm (4-mil)-thick Kapton film layers. The Kapton has a breakdown voltage of approximately 7 kV per 10^{-3}-in. thickness and a dielectric constant of 3.3, which provide good electrical properties. The electrodes were arranged in the asymmetric arrangement illustrated in Fig. 2. They were overlapped by a small amount (approximately 1 mm) to ensure a uniform plasma in the spanwise direction. The plasma actuator was bonded directly to the surface of the model. At the leading edge, where the flow is sensitive to the nose radius, a 0.1-mm recess was molded into the model to secure the actuator flush to the surface. The electrodes were positioned so that the junction between the exposed and covered electrodes was precisely at the leading edge. The actuator induced an accelerating velocity component in the mean freestream direction over the suction surface of the model.

The leading-edge plasma actuator located at $x/c = 0.0$ was operated in an unsteady manner. The ac carrier frequency supplied to the electrodes was 5 kHz and the ac voltage supplied to the electrodes was on the order of 3–12 kV_{p-p}. The power used by the actuator was approximately 2–4 W per linear foot of actuator span. The unsteady actuator frequency f_{mod} was determined based on a Strouhal number St relationship $F^+ = 1$. The actuator was operated at a 10 to 12.5% duty cycle.

B.   Plasma-Actuator Electronics

The plasma-actuator electronics gear was composed of three main components: an oscillator (a sine wave generator), a variable-gain power amplifier, and a high-voltage step-up transformer to provide the voltage necessary to generate plasma. Figure 5 shows a schematic of the electronic circuit used to generate the plasma. The oscillator was composed of several sections designed to provide an output of 0.1 to 3.5 V rms with a frequency range of 10 to 65 kHz. It was designed to provide one of four output waveforms: sine, square, triangle, or sawtooth. This portion of the oscillator is referred to as the carrier oscillator. The output of the carrier oscillator was designed to

a)

b)
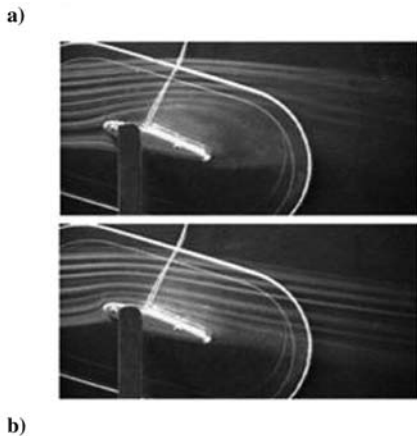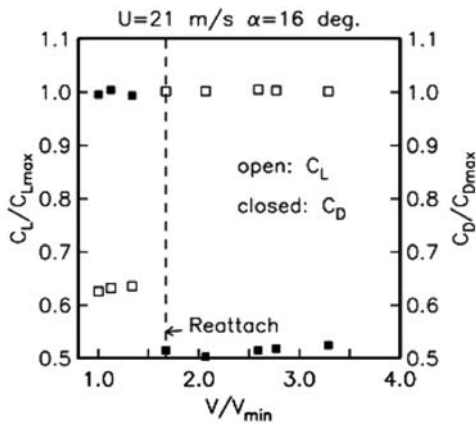
Fig. 6   Results from wind-tunnel experiments conducted on a 2-D NACA 0015: a) lift coefficient versus angle of attack and drag polar for a NACA 0015 airfoil at freestream speeds of 21 m/s with the plasma actuator (left) and results from Corke et al. [15] (right), and b) visualized flow around the airfoil at $\alpha = 16$ deg with leading-edge plasma actuator off (top) and on (bottom) in steady operation; from Post and Corke [15] (flow direction is from left to right).

a)

b)
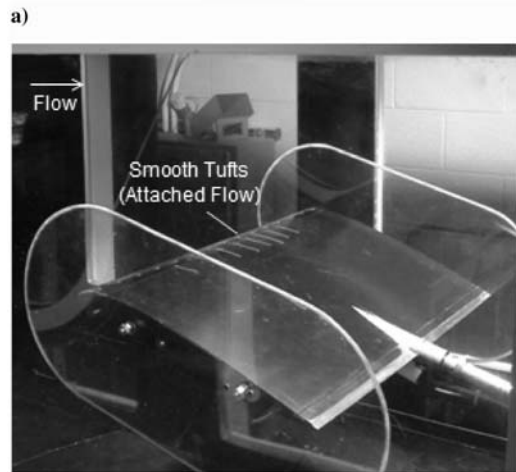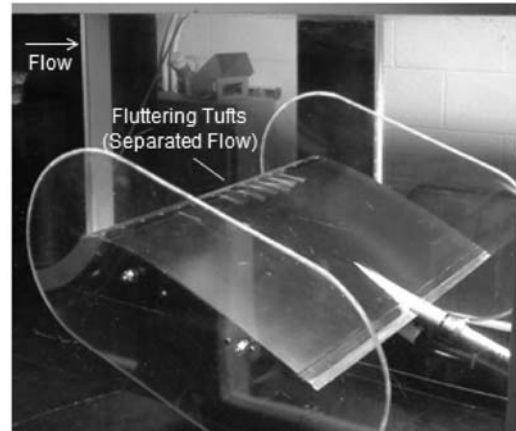
Fig. 7   Photographs showing a comparison of the tufts in separated flow (left) and attached flow (right).

pulse on and off at a rate of 10 to 600 Hz. This on–off pulsing was accomplished through a circuit referred to as the modulation oscillator. The ratio of on-time versus off-time (duty cycle) was also adjustable on the modulation oscillator, with a range of 6.25 to 100%. During the present experiments, the sine waveform at 12.5% duty cycle was used for the unsteady actuation, and the voltage was varied approximately between 3–12 kV_{p-p}. The output of the oscillator controlled a high-speed electronic switch, which enabled the carrier oscillator. All of the adjustments on this oscillator, carrier frequency, modulation frequency, amplitude, and duty cycle were independently adjustable without any interaction between them. A high-voltage probe was used to verify the output to the actuator when deemed necessary.

C. Results

During the wind-tunnel tests the flow speeds ranged from 23 to 60 m/sm with the corresponding Reynolds numbers from 3.83×10^6 to 1.0×10^6 and Mach numbers from 0.06 to 0.176. The test sweep angles ranged from 14 and 24 deg. Table 1 lists all the test cases conducted for this study. The density of air was corrected for the altitude as tests were conducted at $\sim$7000 ft.

With the actuator off, the flow separates at the wing leading edge and a large turbulent separation bubble is formed at the lee side of the model. Unsteady excitation using an unsteady plasma actuator was applied to eliminate or reduce flow separation. Actuator effectiveness was evaluated on the basis of lift enhancement and changes in the pressure measurements made using the high-bandwidth pressure sensors at locations shown in Fig. 2. The results presented here document the ability of the plasma actuators to reattach the flow over a stationary airfoil at high angles of attack,

beyond natural static stall. In a few test cases, the performance of the actuator on a pitching 0015 airfoil at a constant pitch rate of 5 deg /s was also examined, during which only pressure data was collected.

For optimal control (that is, the lowest voltage required to reattach the flow), we set the modulation frequency such that $F^+ = 1$ and slowly increased the actuator voltage while monitoring the lift force and pressure data. A sudden rise in the lift coefficient or a drop in the mean pressure data was indicative of flow reattachment. This technique was successfully used previously to reduce the power required to reattach the flow, as shown in Fig. 6.

Figure 6a shows that once a threshold voltage to the actuator is reached, the flow dramatically reattaches. This was observed as a large increase in the lift and decrease in the drag. The voltage condition in which this occurred is marked by the dashed line in the plot. This was also confirmed using a laser-smoke flow visualization experiment in which flow reattachment is captured clearly, as can be seen in Fig. 6b. Because laser-smoke apparatus is not feasible for high-Reynolds-number flows, we used tufts instead to visualize flow reattachment. An example plot using this approach is shown in Fig. 7. These results are from experiments conducted at a Re_c of 5.17×10^6 and corresponding Mach number of 0.091. Small tufts were placed slightly downstream of the leading-edge actuator, as shown in Fig. 7. Figure 7a shows a photograph of the 0015 airfoil with fluttering tufts, indicative of the separated flow condition, and Fig. 6b shows smooth (nonfluttering) tufts, which indicate flow reattachment or an otherwise dramatic reduction in the separation bubble at the leading edge.

Because monitoring the lift data in real time was not possible, we relied on the pressure-sensor data to confirm the flow reattachment per the preceding logic. Figure 8 shows an overlay of raw pressure data collected from all six pressure sensors at a Re_c of 5.17×10^6 and
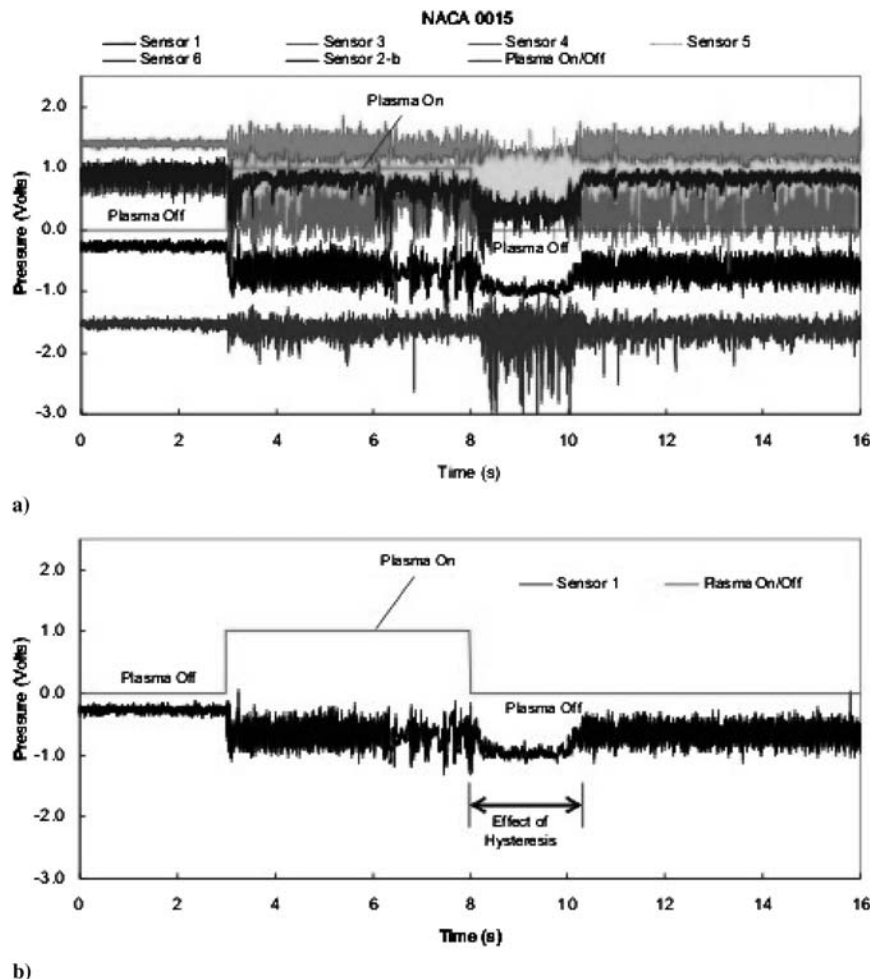

a)

b)

Fig. 8 Overlay of results from pressure measurements showing transient effects of the plasma actuator.

$\alpha = 19$ deg for a period of 16 s, during which the actuator was turned on for approximately 5 s. It was found that pressure sensor 1 located at $x/c = 0.08$, which is closest to the plasma actuator (located at $x/c = 0$), was most sensitive in capturing the actuator-induced flow effects. Our initial speculation, which was experimentally confirmed later, suggested that the turbulence intensity in the separated flowfield downstream of sensor 1 was high enough to offset any noticeable changes from the downstream pressure sensors. In addition, it was found that the actuator was causing partial reattachment of the flow and not full reattachment or elimination of the separation bubble, as evidenced in the modest gains achieved in the lift coefficients (presented later). The control authority was limited by the maximum voltage available (12 kV_{p-p}) to the actuator.

Figures 8b and 9 show the transient response of the plasma actuator captured using sensor 1. A careful examination of these results revealed the effect of flow hysteresis. This is observed by the tendency of the flow to remain attached to the surface even after the actuator was turned off. It is proposed that power can be saved by using a smart control system that is able to use the flow hysteresis.

A comparison of pressure data gathered from two experiments that used different modulation frequencies for the unsteady actuator revealed that for $F^+ = 1$ (Fig. 9a), the flow stays attached for a longer period of time compared with that of $F^+ = 5$ (Fig. 9b). It is hypothesized that operating the actuator at $F^+ = 1$ produces more effective momentum mixing than $F^+ = 5$, thus leading to a longer reattachment time before the effect of the actuator overcomes the hysteresis effect.

Figure 10 shows results from dynamic pitching experiments conducted at a Re_c of 5.17×10^6 and corresponding Mach number of 0.091 and U_∞ of 31 m/s. The airfoil was pitched up and down between 0 and 25 deg at a constant rate of 5 deg/s. During the first run, Figs. 10a and 10b, the actuator was not turned on and baseline data was gathered. Only pressure-sensor data was collected. During

the second run, Figs. 10c and 10d, the actuator was turned on in an unsteady mode at $F^+ = 1$ with a 12.5% duty cycle, between angles of attack of 19 and 25 deg. The effects of the plasma actuator are evident by comparing Figs. 10a–10d. Almost all the sensors in Figs. 10a and 10b reveal slight hysteresis in the flow separation and stall phenomena during pitching cycles, whereas in the case of the plasma actuator, the pitching data shows an increased standard deviation, but symmetrical behavior.

Figure 11 shows the minimum voltage needed to reattach the flow as a function of the forcing frequency F^+ for different poststall angles of attack: $\alpha = 20$, 22, and 24 deg. The α_s for this airfoil was found to be around 18 deg. The forcing frequency was varied between $F^+ = 1$ and 5. Results for Re_c of 4.17×10^5, shown in Fig. 11a, indicate that the minimum voltage condition occurs near $F^+ = 1$, as marked by the vertical line in the plot. It is also observed that as the angle of attack is increased, the minimum voltage to reattach the flow also increases. The voltage to reattach the flow also increased as the forcing frequency moved further away from $F^+ = 1$. Similar trends were observed for Re_c of 5.17×10^5 ($M = 0.091$ and $U_\infty = 31$ m/s). Figure 11c compares the frequency and amplitude effects for different flow speeds (Re_c of 6.67×10^5 and 8.0×10^5) at a fixed angle of attack ($\alpha = 21$ deg and $\alpha_s + 3$ deg). Results show that the minimum voltage to reattach the flow remains the same near $F^+ = 1$; however, as one moves away from $F^+ = 1$, there was a sharp rise in the voltage needed for flow reattachment.

Figure 12 shows trends in the voltage required to reattach the flow as a function of Reynolds number for the 0015 airfoil at $\alpha = 18$ and 20 deg. For these poststall angles of attack, it is observed that the voltage amplitude decreases with increasing Re_c. Later experiments confirmed similar trends for other airfoil section shapes; however, a dependency on the nose radius and maximum t/c was revealed.

Figures 13–15 show changes in the lift coefficients as a function of angle of attack for different Re_c and amplitude settings. It is observed that the effect of plasma actuators are negligible for all angles leading
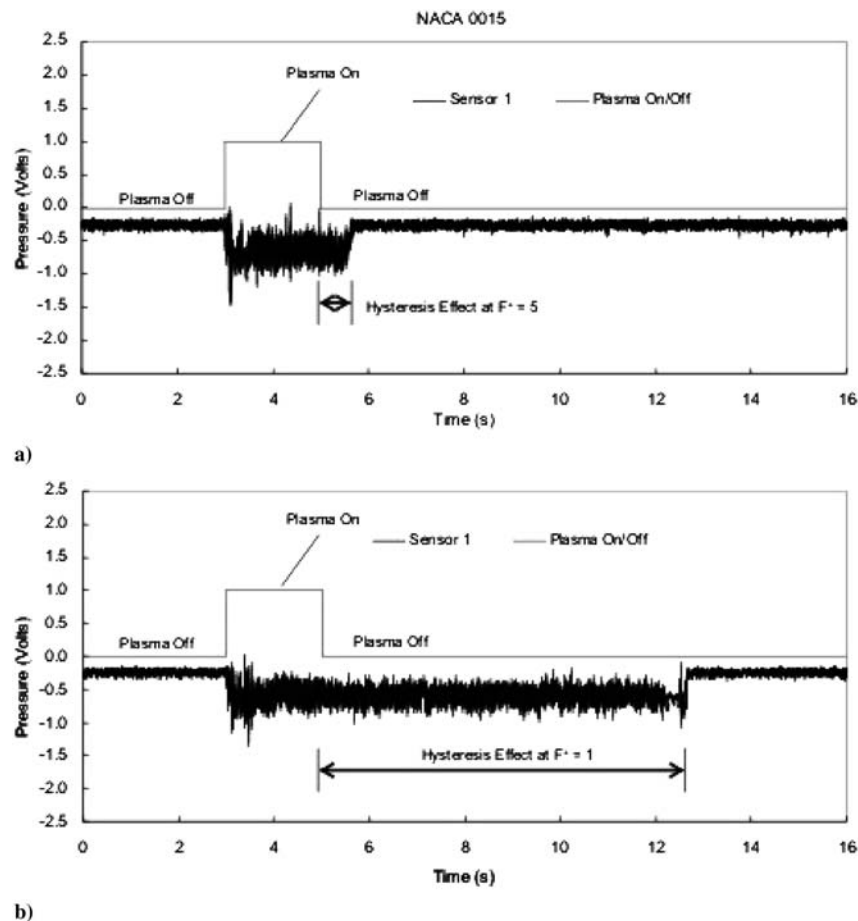

a)

b)

Fig. 9   Results from pressure sensor 1 showing transient effects of the plasma actuator coupled with flow hysteresis.
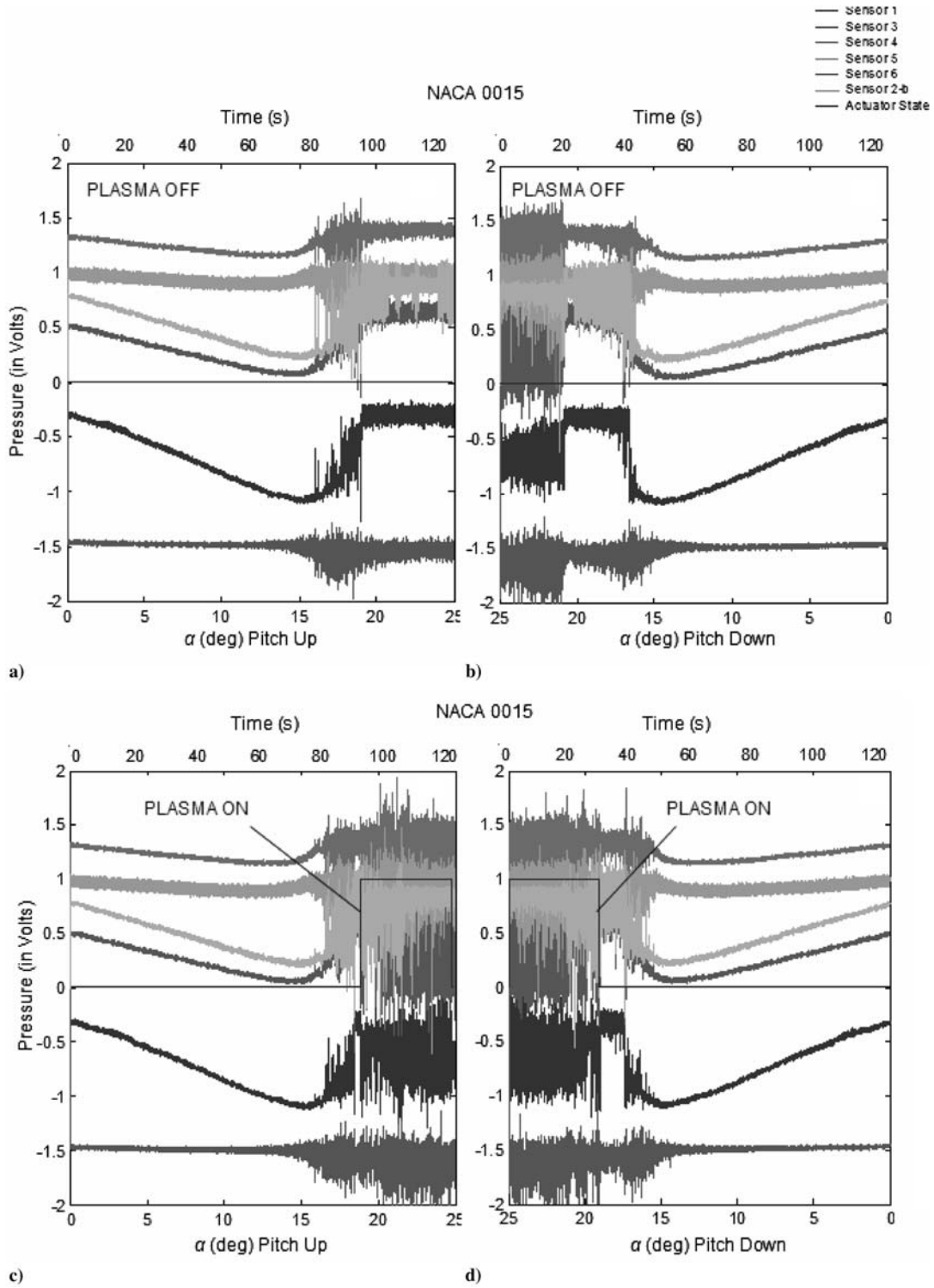
Fig. 10   Overlay of results from pressure measurements from pitching airfoil experiments with actuator off (top) and actuator on (bottom).

up to α_s; however, in the poststall regime, a considerable rise in the lift coefficient is observed with the exception of $\alpha = 19$ or 20 deg in some cases. It is believed that for these small poststall angles, the modulation frequency was not optimal, because the length of the separation bubble was not the full chord length. Increasing the angle of attack further causes the flow to fully separate from the leading edge, and thus the extent of flow separation is equal to the chord length of the airfoil that is used to determine the forcing frequency.

Figure 14 shows that increasing the amplitude of the actuator increases its ability to cause changes in the poststall lift characteristics. This is highlighted in Fig. 14b. Figure 15 shows modest gains in the lift coefficient using the plasma actuator in the

poststall regime for Re_c of 6.09×10^5, 6.67×10^5, and 7.50×10^5. In all these cases in Figs. 13–15, the actuator was operated at $F^+ = 1$. Figure 16 shows changes in the time-averaged pressure data using sensor 1 when the actuator is operated at $F^+ = 1$ for Re_c of 6.09×10^5, 7.50×10^5, 9.17×10^5, and 1.0×10^6.

IV.   Leading-Edge Separation-Control Scaling: NACA 0006, 0015, and 0021

In a parallel effort to study the scaling of leading-edge separation control using plasma actuators, a series of airfoil models were constructed. These models were all NACA four-digit profiles having
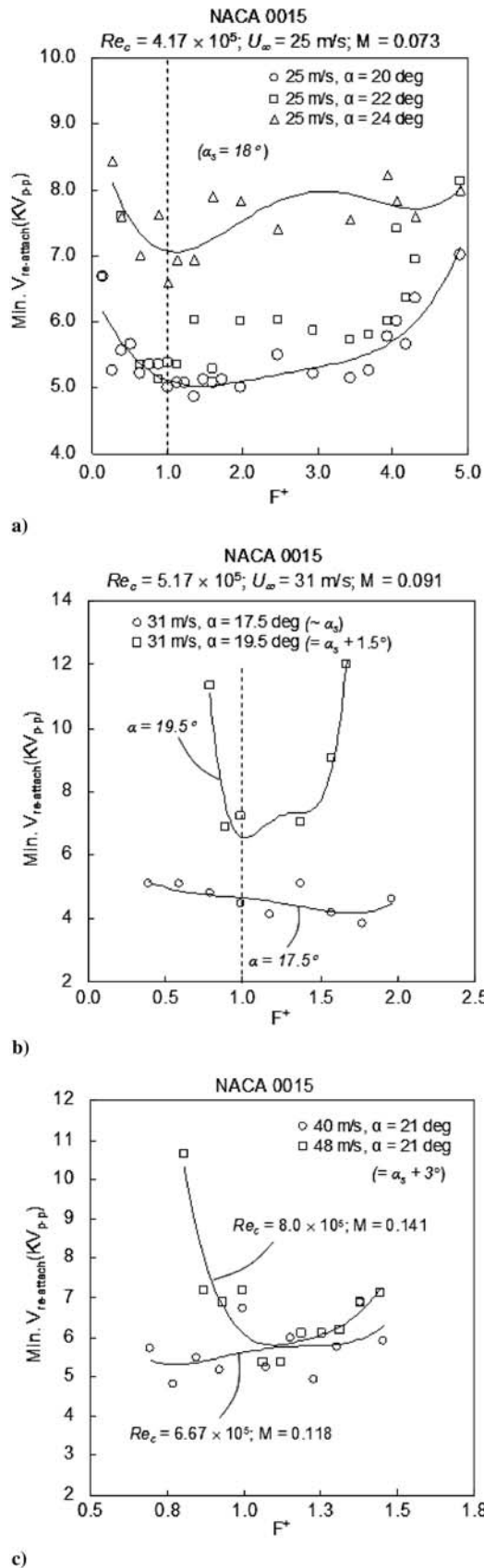
Fig. 11   Minimum voltage required to reattach the leading-edge flow as a function of forcing frequency, flow speed and angles of attack.
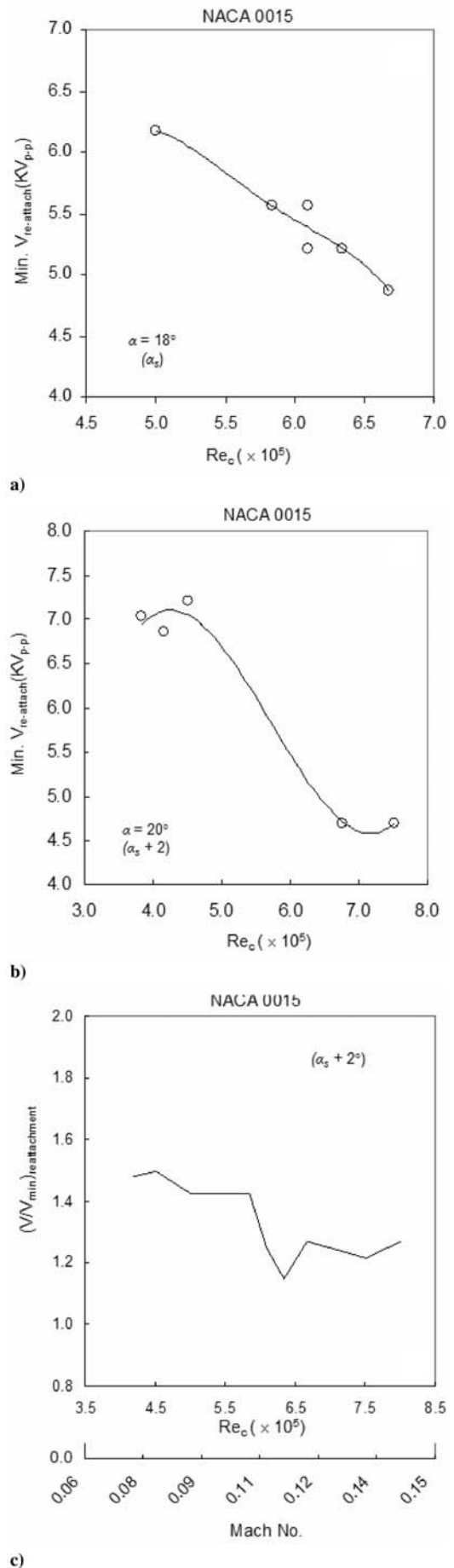

Fig. 12   Minimum voltage needed to reattach flow as a function of flow speed for different angles of attack poststall.
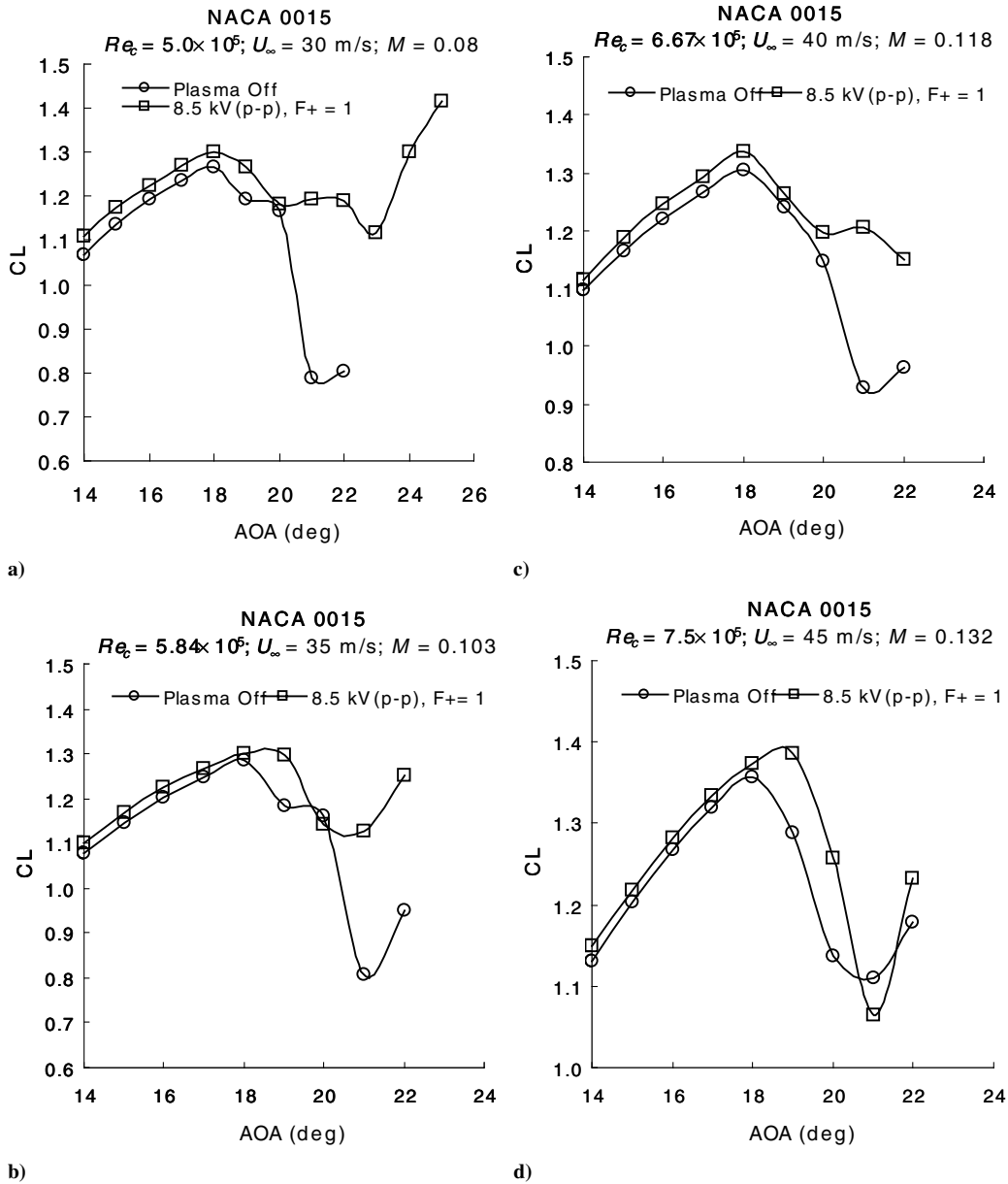
NACA 0015
$Re_c = 5.0 \times 10^5$; $U_\infty = 30$ m/s; $M = 0.08$

a)

NACA 0015
$Re_c = 6.67 \times 10^5$; $U_\infty = 40$ m/s; $M = 0.118$

c)

NACA 0015
$Re_c = 5.84 \times 10^5$; $U_\infty = 35$ m/s; $M = 0.103$

b)

NACA 0015
$Re_c = 7.5 \times 10^5$; $U_\infty = 45$ m/s; $M = 0.132$

d)

Fig. 13 Lift coefficients as a function of angles of attack for different flow speeds with actuator off and actuator on.

maximum thickness-to-chord t/c ratios of 6, 15, and 21%. The profiles all had zero camber. Thus, the airfoils were NACA 0006, 0015, and 0021 profiles. The advantage of using NACA four-digit airfoils was that there was a direct relation between the t/c and the leading-edge radius r_{LE}, which was

$$\frac{r_{LE}}{c} = 1.1019\left(\frac{t}{c}\right) \qquad (1)$$

This allowed us to investigate the effect of the leading-edge radius and thereby the leading-edge Reynolds number as a parameter affecting leading-edge flow reattachment with the plasma actuator.
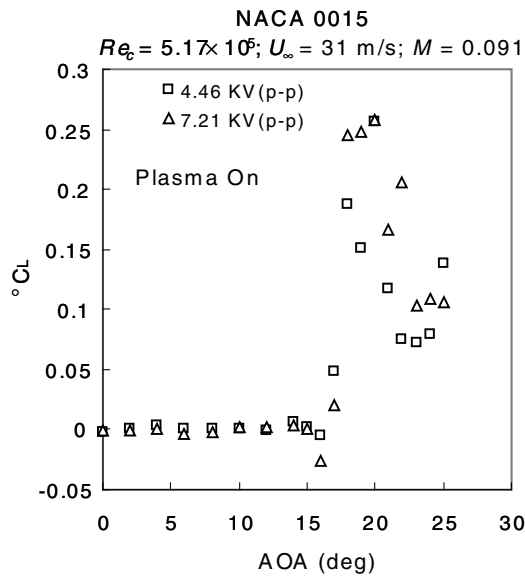
A. Experimental Setup

In this study, each of the models were cast from numerically machined molds in a two-part epoxy mixed with glass microspheres. The chord length of the airfoils was the same and equal to 12.7 cm (5 in.). The span length of the airfoils was 30.48 cm (12 in.). The size of the airfoil was a balance between minimizing blockage effects, especially at the large angles of attack that were investigated, and
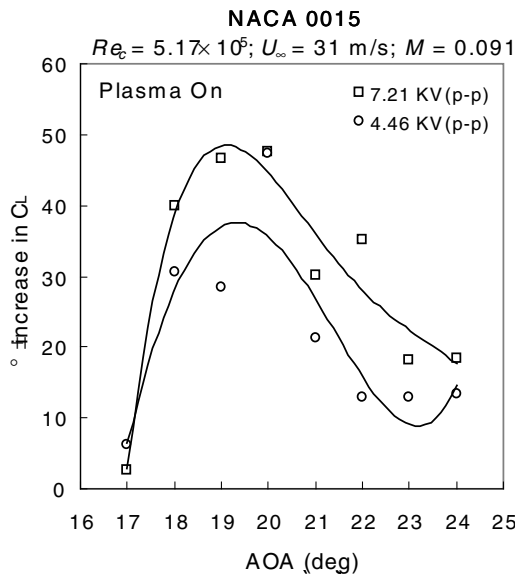
maintaining a large enough chord Reynolds number. At the largest angle of attack of 23 deg, the blockage was 8.5%, which still ultimately required correction for the blockage in the measured lift and drag coefficients.

These experiments were conducted in one of the subsonic wind tunnels in the Center for Flow Physics and Control (FlowPAC) in the Hessert Laboratory at the University of Notre Dame. The facility is an open-return draw-down wind tunnel with a 0.421-m (1.39-ft)-square by 1.8-m (6-ft)-long test section. The tunnel consists of a removable inlet having a series of 12 screens followed by a 24:1 contraction that attaches to the test section. The test section is equipped with a clear Plexiglas sidewall that allows optical access to view the model. The back wall of the test section has removable panels to allow access into the test section.

The airfoils were mounted on the support sting of a lift–drag force balance. The force balance was mounted on the top of the test section. A photograph of the force balance with the airfoil in the test section is shown in Fig. 17. The airfoil was suspended between end plates that were attached to the ceiling and floor of the test section. The end plates were designed to produce a two-dimensional flow around the airfoil. A hole in the ceiling end plate accommodated the sting supporting the airfoil. A hole in the floor end plate allowed
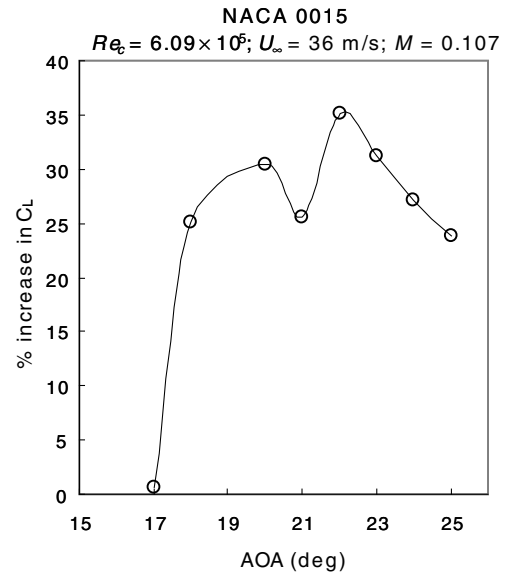
NACA 0015
$Re_c = 5.17 \times 10^5$; $U_\infty = 31$ m/s; $M = 0.091$

a)

NACA 0015
$Re_c = 6.09 \times 10^5$; $U_\infty = 36$ m/s; $M = 0.107$

a)

NACA 0015
$Re_c = 5.17 \times 10^5$; $U_\infty = 31$ m/s; $M = 0.091$

b)

Fig. 14 Changes in the lift coefficient as a function of angle of attack with actuator on.

NACA 0015
Plasma On, $F^+ = 1$

b)

Fig. 15 Percent increase in the lift coefficient as a function of angle of attack with actuator on for different flow speeds.

access to the actuator wiring. This hole was aligned with the support sting so that it would not interfere with angular positioning of the airfoil when setting different angles of attack. A stepper motor on the force balance drove the angular position of the support sting. Its motion was controlled by the data acquisition computer through software. With this, the angular position was repeatable to within 0.005 deg.
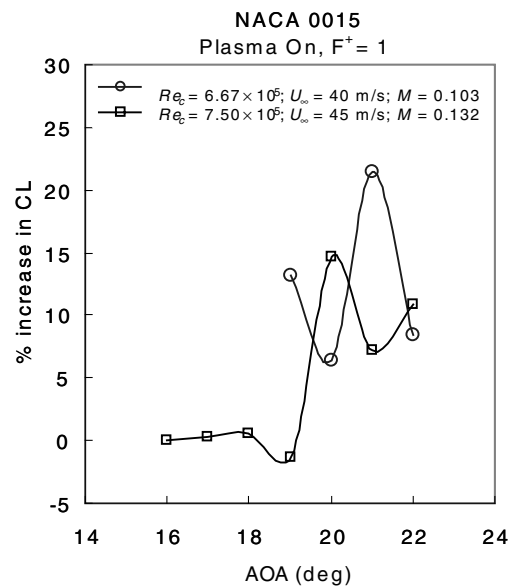
The force balance used a strain-gauge bridge to provide voltage outputs proportional to the respective lift and drag forces. Calibration of the force balance was done by applying known weights to a cable pulley system attached to the support sting.

The measurements were performed over a range of freestream speeds from 17 to 30 m/s. This gave a range of chord Reynolds numbers from 0.380×10^6 to 0.680×10^6. The chord Reynolds numbers corrected for blockage were approximately 20% higher, or from 0.458×10^6 to 0.820×10^6.

The plasma actuator consisted of two copper electrodes separated by two 2-mil-thick Kapton film layers. The electrodes were made from 0.0254-mm-thick copper foil tape. The electrodes were arranged in the asymmetric arrangement that would induce flow toward the suction surface of the airfoil at positive angles of attack.

They were overlapped by a small amount (on the order of 1 mm), to ensure a uniform plasma in the full spanwise direction.

The plasma actuator was bonded directly to the surface of the airfoil. At the leading edge, where the flow is sensitive to the nose radius, a 4-mil-thick recess was molded into the model to accept the actuator and produce a smooth flush surface that maintained the original NACA four-digit airfoil shape.

B. Experimental Approach

Baseline measurements of the lift and drag characteristics of each of the airfoils were first performed. For these, the plasma actuator was installed on the leading edge, but it was not operated. There were two purposes for these measurements. The first was to determine that the airfoils displayed the proper linear lift versus angle-of-attack region at lower angles and that the lift-coefficient slope $dC_l/d\alpha = 2\pi$. This indicated that the airfoils were accurately molded. The second purpose of the baseline measurements was to determine the angle of attack at which the airfoils reached the maximum lift and subsequently stalled, α_s.
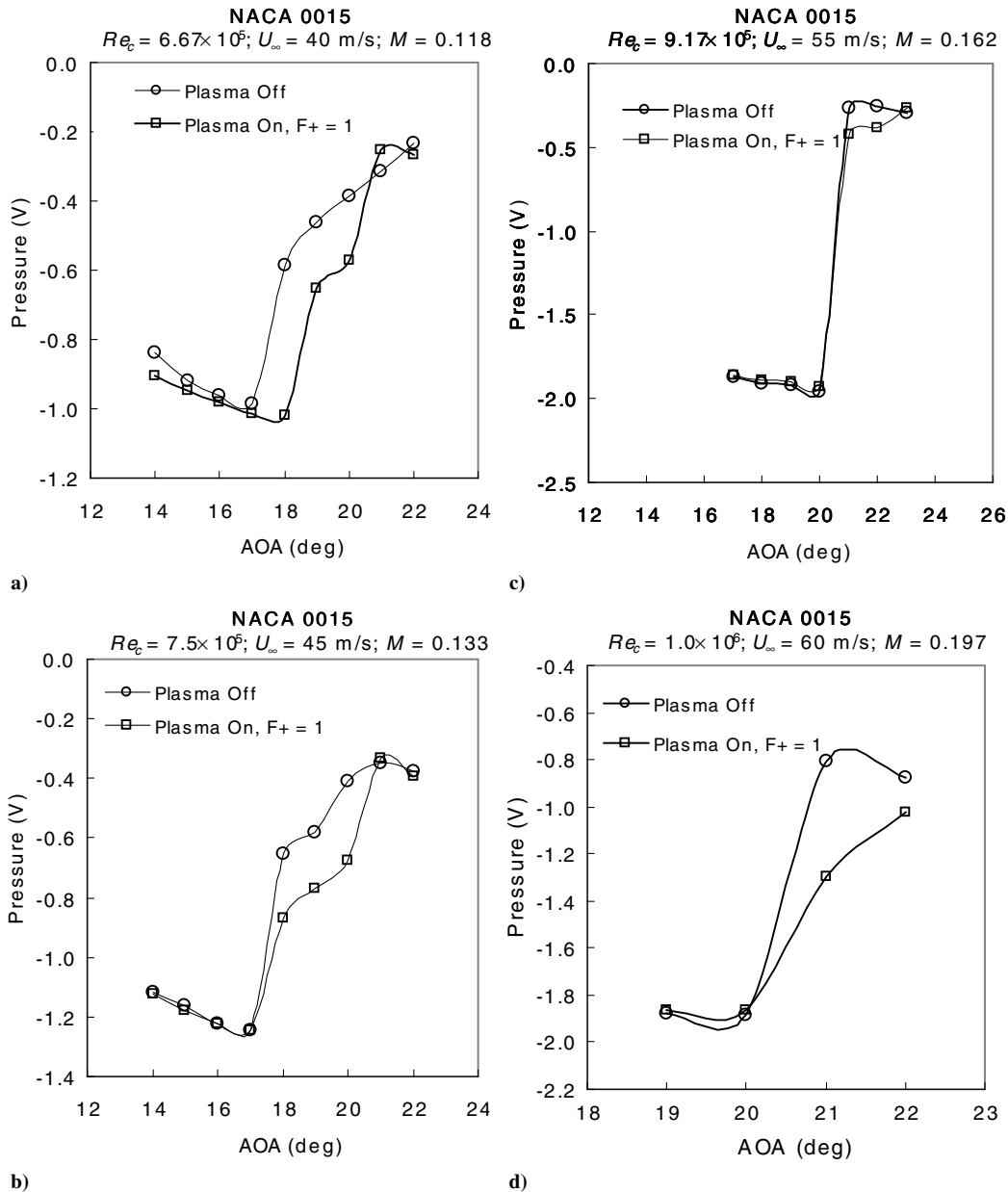
Fig. 16   Changes in the time-averaged pressure data as a function of angles of attack for different flow speeds with actuator off and actuator on.

The baseline measurements were conducted at six freestream velocities of 17, 20, 22, 25, 27, and 30 m/s. The values of the stall angle of attack were found to depend on the airfoil t/c as well as to increase slightly with increasing Reynolds number for the same airfoil. Therefore, the characteristics of the plasma actuator to reattach the flow were referenced to the *poststall* angle of attack of $\alpha_s + \alpha$ for each profile and Reynolds number.

Once the baseline characteristics of each airfoil had been established, the following procedure was performed:

1) One of the airfoils was mounted on the lift–drag balance.

2) A freestream speed was set and the airfoil was placed at a poststall angle of attack of $\alpha_s + \alpha$.

3) The actuator was operated at an unsteady frequency f that corresponded to $F^+ = fc/U_\infty = 1$, and the amplitude to the actuator was increased until the separated leading-edge flow reattached. The flow reattachment was verified in real time by monitoring the voltage output proportional to the lift. The flow reattachment appeared as a step-change increase in the lift. The voltage supplied to the plasma actuator when the flow first reattached was defined as $V_{\text{reattachment}}$.

4) The freestream speed was changed and the process was repeated.

The procedure was performed for the three airfoils at the six freestream speeds. The results were then accumulated. Figures 18–20 plot the effect of the chord Reynolds number on $V_{\text{reattachment}}$ for the range of poststall angles of attacks.

C.   Results

Figure 18 shows the results for the NACA 0006 airfoil. The curves are a smooth spline fit through the measured points. The symbols signify which curves apply to the different poststall angles of attack. Similar results for the NACA 0015 airfoil are presented in Fig. 19 and for the NACA 0021 airfoil are presented in Fig. 20. From these, we observe three general features:

1) The minimum actuator voltage $V_{\text{reattachment}}$ required to reattach the flow increases with an increase in the poststall angle of attack.

2) The change in voltage required to reattach the flow with increasing poststall angle of attack increases with increasing t/c, with the voltages required for the NACA 0021 being approximately twice those of the NACA 0006.

3) Over the range of chord Reynolds numbers investigated, there is, at most, a *weak dependence of Reynolds number* on $V_{\text{reattachment}}$.
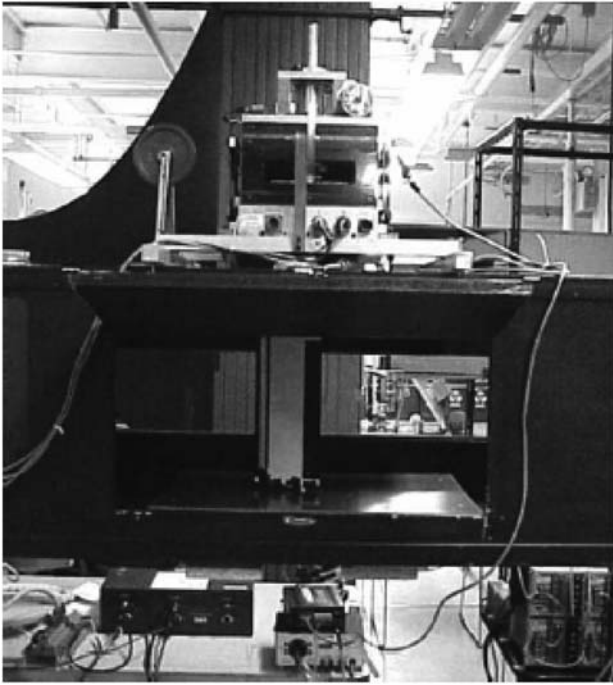
Fig. 17 Photograph of one of the airfoil models mounted on the lift–drag balance in the wind-tunnel test section at the University of Notre Dame.
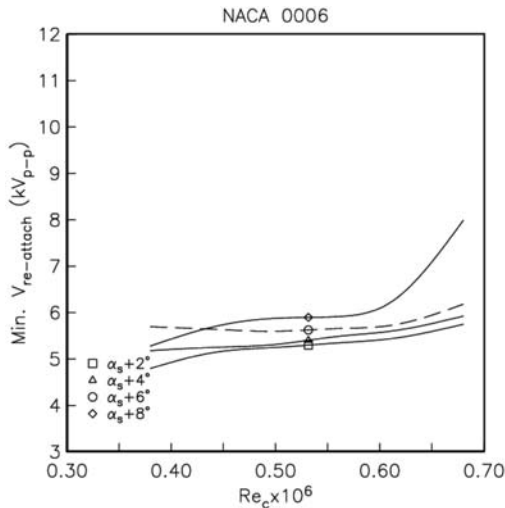

Fig. 18 Minimum plasma-actuator voltage required to reattach leading-edge flow separation of NACA 0006 airfoil as a function of chord Reynolds number for different poststall angles of attack.

Fig. 19 Minimum plasma-actuator voltage required to reattach leading-edge flow separation of NACA 0015 airfoil as a function of chord Reynolds number for different poststall angles of attack.

Fig. 20 Minimum plasma-actuator voltage required to reattach leading-edge flow separation of NACA 0021 airfoil as a function of chord Reynolds number for different poststall angles of attack.

Given the weak dependence of $V_{reattachment}$ on the Reynolds number, the data were plotted to highlight the dependence on the poststall angle of attack. This is shown in Figs. 21–23. Figure 21 shows the results for the NACA 0006 airfoil. At each poststall angle of attack, the symbols correspond to the different chord Reynolds. To obtain the trend of $V_{reattachment}$ as a function of the poststall angle of attack, a least-squares-error curve fit was performed between points made up of the average of the $V_{reattachment}$ values for the Reynolds numbers at each $\alpha_s + \alpha$ point. The curves shown in Figs. 21–23 represent linear best-fit curves of the respective minimum voltages to reattach the flow as a function of the poststall angle of attack. These linear fits were replotted for all three thickness-to-chord-ratio airfoils in Fig. 24.

Figure 24 indicates that the minimum voltage at the lowest poststall angle of attack is approximately the same for the three t/c ratios, but the change with angle of attack increases as t/c increases.
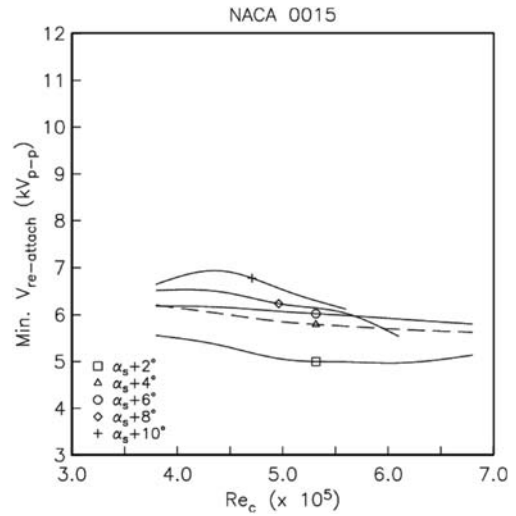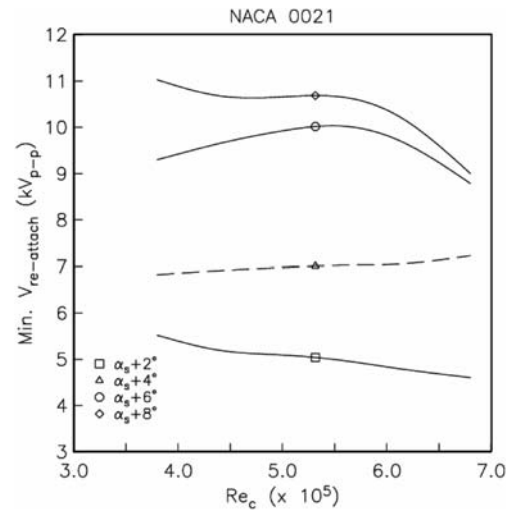
The premise is that $V_{reattachment}$ scales with the leading-edge radius r_{LE}. To check this, the slope of the line for the NACA 0015 was scaled to that of the NACA 0021 based on the ratio of their leading-edge radii. The result suggests that the difference in the slope is proportional to the square of the ratio of the leading-edge radii. This is shown as the line segment labeled as

$$(\text{slope } 0015) \times \left(\frac{(r_{LE})_{21}}{(r_{LE})_{15}}\right)^2 \tag{2}$$

where the ratio of the leading-edge radii are based on Eq. (1).

If the same scaling is applied between the NACA 0015 and 0006 airfoils, the slope labeled as

$$(\text{slope } 0015) \times \left(\frac{(r_{LE})_6}{(r_{LE})_{15}}\right)^2 \tag{3}$$

is obtained. This slope is somewhat smaller than shown for the 0006 airfoil in the figure. We suspect that the physically very small radius on this airfoil was increased slightly by the addition of the Kapton film for the actuator. Therefore, the behavior was more like an airfoil with a slightly larger leading-edge radius. This radius was still smaller than that of the 0015 airfoil, because its slope is smaller.
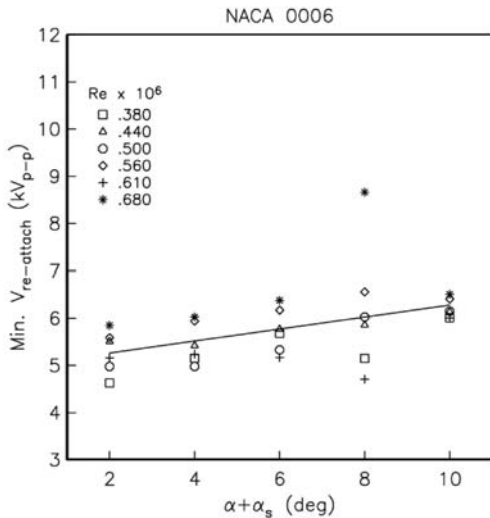
Fig. 21 Minimum plasma-actuator voltage required to reattach leading-edge flow separation of NACA 0006 airfoil as a function of poststall angle of attack for different chord Reynolds numbers.
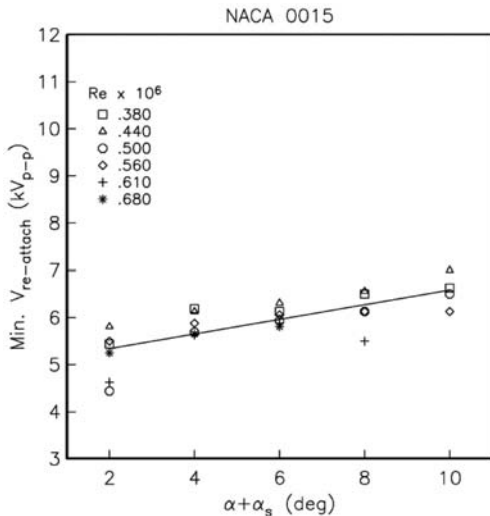

Fig. 22 Minimum plasma-actuator voltage required to reattach leading-edge flow separation of NACA 0015 airfoil as a function of poststall angle of attack for different chord Reynolds numbers.
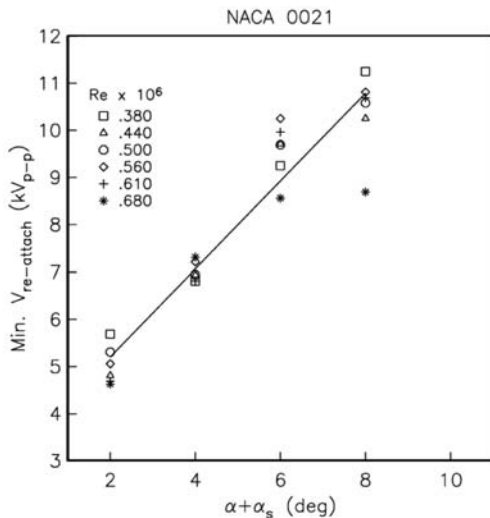

Fig. 23 Minimum plasma-actuator voltage required to reattach leading-edge flow separation of NACA 0021 airfoil as a function of poststall angle of attack for different chord Reynolds numbers.
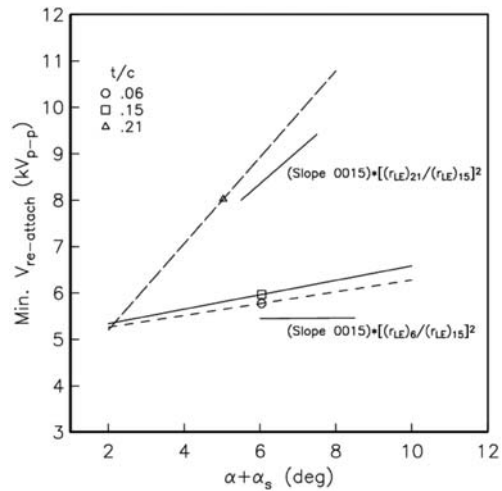

Fig. 24 Minimum plasma-actuator voltage required to reattach leading-edge flow separation as a function of poststall angle of attack for three thickness-to-chord ratios.

V. Conclusions

Summarizing the results for leading-edge plasma actuators designed to increase the stall angle of attack, for $0.380 \times 10^6 \leq Re_c \leq 0.680 \times 10^6$ and 2 deg $\leq (\alpha_s + \alpha) \leq 10$ deg, the voltage required to reattach the flow was 1) only weakly dependent on chord Reynolds number, 2) strongly dependent on the poststall angle of attack, and 3) scaled with the square of the radius of the leading edge.

Future plans include wind-tunnel testing and flight experimentation on the use of plasma actuators for aerodynamic enhancement of different wing geometries at Reynolds numbers typical of aircraft takeoff and landing speeds.

References

[1] Corke, T., and Post, M., "Overview of Plasma Actuators: Concepts, Optimization, and Applications," AIAA Paper 2005-0563, Jan. 2004.

[2] Roth, J. R., "Aerodynamic Flow Acceleration Using Paraelectric and Peristaltic Electrohydrodynamic Effects of a One Atmosphere Uniform Glow Discharge Plasma," *Physics of Plasmas*, Vol. 10, No. 5, 2003, pp. 2117–2126.
doi:10.1063/1.1564823

[3] Kimmel, R. L., Hayes, J. R., Menart, J. A., and Shang, J., "Effect of Surface Plasma Discharges on Boundary Layers at Mach 5," AIAA Paper 2004-0509, Jan. 2004.

[4] Merriman, S., Ploenjes, E., Palm, P., and Admovich, I., "Shock Wave Control by Nonequilibrium Plasmas in Cold Supersonic Gas Flows," *AIAA Journal*, Vol. 39, No. 8, Aug. 2001.

[5] Samimy, M., Adamovich, I., Webb, B., Kastner, J., Hileman, J., Keshav, S., and Palm, P., "Development and Characterization of Plasma Actuators for High Speed Jet Control," *Experiments in Fluids*, Vol. 37, No. 4, 2004, pp. 577–588.
doi:10.1007/s00348-004-0854-7

[6] Suchomel, C., Van Wie, D., and Risha, D., "Perspectives on Cataloguing Plasma Technologies Applied to Aeronautical Sciences," AIAA Paper 2003-3852, June 2003.

[7] Enloe, L., McLaughlin, T., Van Dyken, R., Kachner, K. D., Jumper, E., Corke, T., Post, M., and Haddad, O., "Mechanisms and Response of a Single Dielectric Barrier Plasma Actuator: Geometric Effects," *AIAA Journal*, Vol. 42, No. 3, Mar. 2004, pp. 595–604.

[8] Enloe, L., McLaughlin, T., Van Dyken, R., Kachner, K. D., Jumper, E., and Corke, T., "Mechanisms and Response of a Single Dielectric Barrier Plasma Actuator: Plasma Morphology," *AIAA Journal*, Vol. 42, No. 3, Mar. 2004, pp. 589–594.

[9] Orlov, D. M., and Corke, T. C., "Numerical Simulation of Aerodynamic Plasma Actuator Effects," AIAA Paper 2005-1083, Jan. 2005.

[10] Nelson, C. C., Cain, A. B., Patel, M. P., and Corke, T. C., "Simulation of Plasma Actuators Using the Wind-US Code," AIAA Paper 2006-0634, Jan. 2006.

[11] Orlov, D. M., Corke, T. C., and Patel, M. P., "Electric Circuit Model for the Aerodynamic Plasma Actuator," AIAA Paper 2006-1206, Jan. 2006.

[12] Roth, J. R., Sherman, D. M., and Wilkinson, S. R., "Electro-hydrodynamic Flow Control with a Glow-Discharge Surface Plasma," *AIAA Journal*, Vol. 38, No. 7, July 2000.

[13] Corke, T., Jumper, E., Post, M., Orlov, D., and McLaughlin, T., "Application of Weakly Ionized Plasmas as Wing Flow-Control Devices," AIAA Paper 2002-0350, Jan. 2002.

[14] Huang, J., Corke, T., and Thomas, F., "Plasma Actuators for Separation Control of Low-Pressure Turbine Blades," AIAA Paper 2003-1027, Jan. 2003.

[15] Post, M. L., and Corke, T. C., "Separation Control on High Angle of Attack Airfoil Using Plasma Actuators," AIAA Paper 2003-1024, Jan. 2003.

[16] Corke, T. C., and Matlis, E., "Phased Plasma Arrays for Unsteady Flow Control," AIAA Paper 2000-2323, Jan. 2000.

[17] Post, M., and Corke, T., "Separation Control Using Plasma Actuators—Stationary and Oscillating Airfoils," AIAA Paper 2004-0841, Jan. 2004.

[18] Corke, T., He, C., and Patel, M., "Plasma Flaps and Slats: An Application of Weakly Ionized Plasma Actuators," AIAA Paper 2004-2127, June 2004.

[19] Patel, M. P., Sowle, Z. H., Corke, T. C., and He, C., "Autonomous Sensing and Control of Wing Stall Using a Smart Plasma Slat," *Journal of Aircraft*, Vol. 44, No. 2, Mar.–Apr. 2007, pp. 516–527.
doi:10.2514/1.24057

[20] Patel, M. P., Ng, T. T., Vasudevan, S., Corke, T. C., and He, C., "Plasma Actuators for Hingeless Aerodynamic Control of an Unmanned Air Vehicle," *Journal of Aircraft*, Vol. 44, No. 4, July–Aug. 2007, pp. 1264–1274.
doi:10.2514/1.25368

[21] Nelson, R. C., Corke, T. C., Otham, H., Matsuno, T., Patel, M. P., and Ng, T. T., "Modification of the Flow Structure over a UAV Wing for Roll Control," AIAA Paper 2007-884, Jan. 2007.

[22] Lopera, J., Ng, T. T., Patel, M. P., Vasudevan, S., and Corke, T. C., "Aerodynamic Control of 1303 UAV Using Windward Surface Plasma Actuators," AIAA Paper 2007-636, Jan. 2007.

[23] Seifert, A., Bachar, T., Moss, D., Shepshelovish, M., and Wygnanski, I., "Oscillatory Blowing: A Tool to Delay Boundary-Layer Separation," *AIAA Journal*, Vol. 11, No. 31, 1993, pp. 2052–2060.

[24] Seifert, A., Darabi, A., and Wygnanski, I., "Delay of Airfoil Stall by Periodic Excitation," *Journal of Aircraft*, Vol. 33, No. 4, 1996, pp. 691–698.

[25] Seifert, A., Eliahu, S., and Greenblatt, D., "Use of Piezoelectric Actuators for Airfoil Separation Control," *AIAA Journal*, Vol. 36, No. 8, 1998, pp. 1535–1537.

[26] Seifert, A., and Pack, L., "Oscillatory Excitation of Unsteady Compressible Flows over Airfoils at Flight Reynolds Numbers," AIAA Paper 1999-0925, 1999.

[27] Greenblatt, D., and Wygnanski, I., "The Control of Separation by Period Excitation," *Progress in Aerospace Sciences*, Vol. 36, 2000, pp. 487–545.
doi:10.1016/S0376-0421(00)00008-7

[28] Corke, T. C., Hertz, B., and Patel, M. P., "Plasma Flow Control Optimized Airfoil," AIAA Paper 2006-1208, Jan. 2006.

[29] Post, M., Grothe, R. L., Wood, K. L., Corke, T. C., and Patel, M. P., "Scaling Effects of Aerodynamic Plasma Actuators on a HSNLF Airfoil," AIAA Paper 2007-0638, Jan. 2007.